nature research

https://doi.org/10.1038/s41566-020-0677-y

Supplementary information

Sub-nanometre resolution in single-molecule photoluminescence imaging

In the format provided by the authors and unedited

Supplementary Information for

Sub-nanometre resolution in single-molecule photoluminescence imaging

Ben Yang[1†], Gong Chen[1†], Atif Ghafoor[1], Yufan Zhang[1], Yao Zhang[1], Yang Zhang[1*], Yi Luo[1], Jinlong Yang[1], Vahid Sandoghdar[2], Javier Aizpurua[3], Zhenchao Dong[1*] and J. G. Hou[1*]

[1] Hefei National Laboratory for Physical Sciences at the Microscale and Synergetic Innovation Centre of Quantum Information & Quantum Physics, University of Science and Technology of China, Hefei, Anhui 230026, China

[2] Max Planck Institute for the Science of Light, Erlangen 91058, Germany

[3] Materials Physics Centre CSIC-UPV/EHU and Donostia International Physics Centre DIPC, Paseo Manuel de Lardizabal, Donostia-San Sebastián 20018, Spain.

[†]These authors contributed equally to this work.

[*]Corresponding authors.

[*]emails: zhyangnano@ustc.edu.cn; zcdong@ustc.edu.cn; jghou@ustc.edu.cn.

Contents

S1 About the fabrication of a TEPL-active silver tip

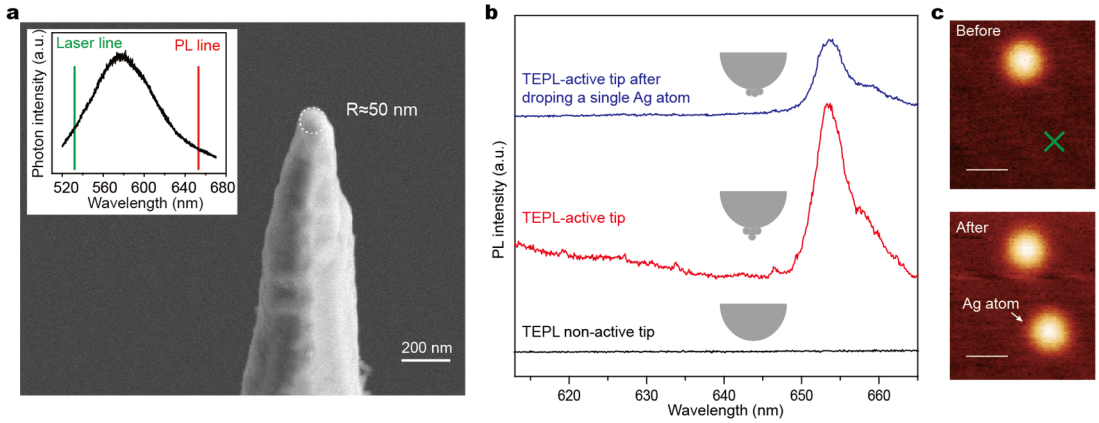

Figure S1 | Characterizations on silver tips used in our experiments. a, SEM image of a typical Ag tip after electrochemical etching. The inset is a typical nanocavity plasmon emission spectrum acquired by STM-induced luminescence for a Ag tip on 3ML-NaCl/Ag(100) (acquisition condition: –2.5 V, 0.5 nA, 20 s). **b**, Nanocavity enhanced PL spectra above a single ZnPc molecule on 3ML-NaCl/Ag(100) for three different tip conditions: initial TEPL non-active tip (bottom), strong TEPL active-tip (middle) and weak TEPL-active tip (top) (acquisition condition: 532 nm, 0.2 mW, –1 V, 2 pA, 30 s). The schematics in the insets show three possible corresponding tip structures. **c**, STM images before and after controlled tip–substrate contact experiment. Scale bar: 1 nm.

The silver (Ag) tips used in our experiments were first prepared by electrochemical etching[1]. As shown in Fig. S1a, the typical radius of the etched tip apex is about 50 nm, which is also consistent with previous reports[2,3]. After introducing into the UHV chamber, the as-etched Ag tips were usually treated by argon-ion sputtering and electron-bombarding to achieve clean and smooth tip apexes. Then, the tips were further transferred to the STM scanning stage for single-molecule TEPL measurements. Generally speaking, in the initial situation without further tip treatments, no TEPL signal from molecules can be detected, as shown in the black curve of Fig. S1b. This kind of tips are tagged as TEPL non-active tips and are believed to have a relatively blunt tip apex. Finally, the tip apex was fine-modified through cycles of controlled and

gentle tip indentations to the Ag substrate, which can re-shape the nanocavity plasmon mode and make it to resonate with both the laser excitation and PL emission, as exemplified in the inset of Fig. S1a. The Ag tips thus treated can become TEPL-active and produce strong PL signals from a single molecule, as shown in the red curve of Fig. S1b. Importantly, since Ag atoms or clusters can be transferred to the tip apex during tip indentations, the change of a TEPL non-active tip to a TEPL-active tip is thus attributed to the formation of an atomistic protrusion at the tip apex. Such speculation is supported by the estimation on the effective tip radius (R) down to ~0.5 nm, as discussed in main-text Fig. 2e, and also by theoretical simulations (see Section S6 for details). To further support such a hypothesis, a controlled tip–substrate contact experiment was performed. As shown in Fig. S1c, we can make a controlled tip indentation to the metal substrate via tip Z-manipulation (feedback "off") after estimating the gap distance for a given tunnelling condition (see Section S3 for details). Upon forming a contact, a single Ag atom was found to transfer from the tip to the substrate, leading to the change of the atomic-scale structure at the tip apex and resultant modifications on the TEPL plasmonic enhancement. Indeed, as shown in the blue curve of Fig. S1b, the NCP-enhanced PL signal became evidently weaker. Such spectral evolution strongly suggests that an atomistic protrusion at the tip apex thus engineered is crucial for the realization of NCP-enhanced PL from a single molecule.

Here we would like to make a note on the additional features of the weak peaks shown in main-text Fig. 1c and Fig. S1b above. The dominant emission peak near 653 nm can be clearly assigned to the Q(0,0) transition, while the weak shoulder around 658 nm is believed to associate with the intramolecular vibronic transition and/or phonon wing due to a vibron−phonon interaction with the NaCl substrate layer[4,5]. Nevertheless, an unambiguous assignment of this weak shoulder requires further experimental and theoretical studies. There is also an extremely weak emission band around 626 nm (main-text Fig. 1c), which is probably related to the Q(1,0) “hot-luminescence” coming directly from high-lying vibrational excited states. This is because the laser energy of 532 nm used can excite the molecule directly from the molecular ground state to the

vibrational excited states of the electronic excited state, whose radiative decay rate can be greatly enhanced by the nanocavity plasmon to somewhat compete with the rapid vibrational relaxation[6]. Note that there are also some weak sharp peaks with a linewidth of about 17 cm^{-1} on the spectral profile, which are attributed to the Raman scattering signals.

S2 Estimation on the TEPL enhancement factor

The estimation of the TEPL enhancement factor (EF) is based on the following widely-adopted formula[3]

$$\mathrm{EF} = \frac{I_{\mathrm{near}}}{I_{\mathrm{far}}} \times \frac{N_{\mathrm{far}}}{N_{\mathrm{near}}},$$

where I_{far} is the PL intensity when the tip is fully retracted, I_{near} is the net near-field PL intensity measured above the ZnPc lobe on 3ML-NaCl/Ag(100) under tunnelling conditions (defining a small tip−molecule distance) after subtracting NCP background signals collected above the 3ML-NaCl surface, N_{far} is the number of molecules on 3ML-NaCl/Ag(100) within the area of the laser spot, and N_{near} is the number of molecules within the effective enhancement area of the NCP. As shown in main-text Fig. 1c, the observation of molecule-specific emission for the tip positioned above a single ZnPc, together with the observation of a featureless spectrum obtained for the tip positioned above the bare 3ML-NaCl surface, suggests the molecular fluorescence signals is emitted from the particular single ZnPc underneath the tip and thus $N_{\mathrm{near}} = 1$. N_{far} is estimated based on the coverage of ZnPc molecules on the 3ML-NaCl/Ag(100) surface. According to statistical analyses on STM images, we found that there are on average about 5 ZnPc molecules adorbed on 3ML-NaCl/Ag(100) within an area of 50 nm × 50 nm, corresponding to a coverage density of about 2000 molecules/μm^2. Since the diameter of the focusing laser spot in our system is about 30 μm, there are about 1.4×10^6 ZnPc molecules on the 3ML-NaCl/Ag(100) surface within the laser spot.

The TEPL intensities were measured by a SPAD with a bandpass filter (655 nm ± 7.5 nm). When the tip is fully retracted, the measured far-field photon intensity I_{far} is about 442 Hz (which could come mainly from background noises since the PL spectrum is featureless in this case, showing no molecule-specific emission peaks. In other words, the real far-field PL signal intensity from all ZnPc molecules on 3ML-NaCl/Ag(100) is definitely less than 442 Hz); when the tip is positioned above the lobe of the ZnPc, the measured near-field PL photon intensities I_{near} is about 55 kHz. Thus, even if we conservatively take 442 Hz as the far-field signal, based on the above equation, the EF is estimated to be as high as about 1.7×10^{8}. It is worth noting that such a large enhancement factor refers to the ratio between the PL intensity from a single molecule in a plasmonic nanocavity and that of a single molecule on 3ML-NaCl/Ag(100) without the tip, rather than the comparison with the PL intensity from a single molecule placed in vacuum. The enhancement factor estimated experimentally is in fair agreement with that calculated from theoretical simulations, as detailed in Section S6.6.

S3 Estimation on the gap distance

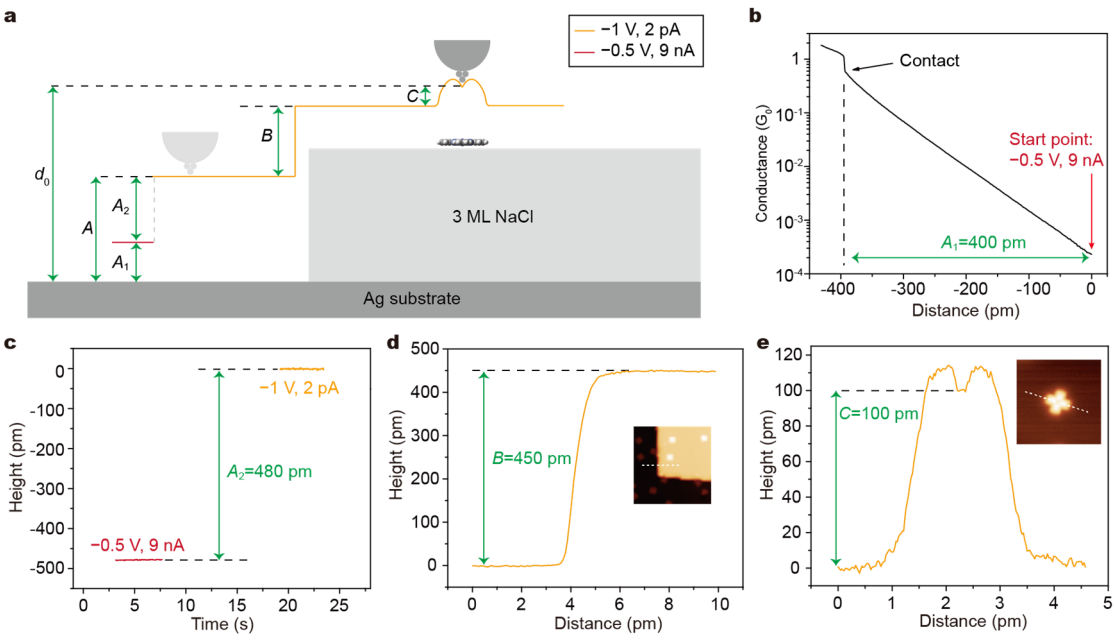

Figure S2 | Gap-distance measurements. a, Schematic illustrating various distances in an

STM junction. **b**, The tip trajectory during the approaching to the Ag substrate from an initial setpoint (−0.5 V, 9 nA) to the contact point. **c**, The distance variation between scanning conditions −1 V, 2 pA and −0.5 V, 9 nA. **d**, The apparent height profile of a 3ML-NaCl island indicated by the dashed white line in the inset. The inset is a STM image of 3ML-NaCl/Ag(100). Scanning condition: −1 V, 2 pA. **e**, The apparent height profile of a single ZnPc molecule on 3ML-NaCl/Ag(100) indicated by the dashed white line in the inset. The inset is a STM image of a single ZnPc molecule on 3ML-NaCl/Ag(100). Scanning condition: −1 V, 2 pA.

The gap distance d_0 shown in main-text Fig. 2a for the set-point tunnelling condition of −1 V and 2 pA is estimated through the measurements of the tip trajectories on the sample with different scanning conditions, as illustrated in Figure S2a. The selection of such a scanning condition (−1 V and 2 pA) as a set-point for spectral measurements (main-text Figs. 1c and 2b) or for photon imaging (main-text Figs. 1d, 2f and 4) was based on the balance between a stable scanning and a strong NCP-enhanced PL intensity. According to the schematic in Fig.S2a, it is evident that $d_0 = A + B + C$, with A, B, and C distances defined in the figure. Since the background electronic noise level of the pre-amplifier is about 10 pA (larger than 2 pA) when its gain was set at a low amplification ratio (10^5 V/A) in order to measure the very large current at the μA range for the moment forming a tip-substrate contact, the measurement of the tip–Ag substrate distance (A) for the tunnelling condition of −1 V and 2 pA was divided into two steps. First, we measured the tip–Ag substrate distance (A_1) at the setpoint of −0.5 V and 9 nA through a controlled tip–substrate contact using the low-gain pre-amplifier setting. As shown in Fig. S2b, a clear rise in the tunnelling current suggests the contact of the tip with the substrate and indicates a tip approaching distance of ~400 pm from the start point (i.e., A_1 is about 400 pm). We then measured the distance difference (A_2) between the tip positions when changing the scanning condition from −0.5 V and 9 nA to −1 V and 2 pA using a high-gain pre-amplifier setting (10^9 V/A). As shown in Fig. S2c, A_2 is about 480 pm. Thus, we can deduce the gap distance between the Ag tip and the Ag substrate is ~880 pm (i.e., $A = A_1 + A_2 = 880$ pm) at the setpoint of −1 V and 2

pA. Then, by using the measured apparent heights of the 3ML NaCl (*B*) and a single ZnPc molecule (*C*) shown in Fig. S2d and S2e, we can estimate the gap distance d_0 between the tip and Ag substrate to be about 1.43 nm (i.e., $d_0 = A + B + C \approx 1430$ pm) when the tip is positioned above the ZnPc centre on 3ML-NaCl/Ag(100) at a tunnelling condition of −1 V and 2 pA.

S4 Evolution of NCP-enhanced single-molecule PL imaging at different gap distances

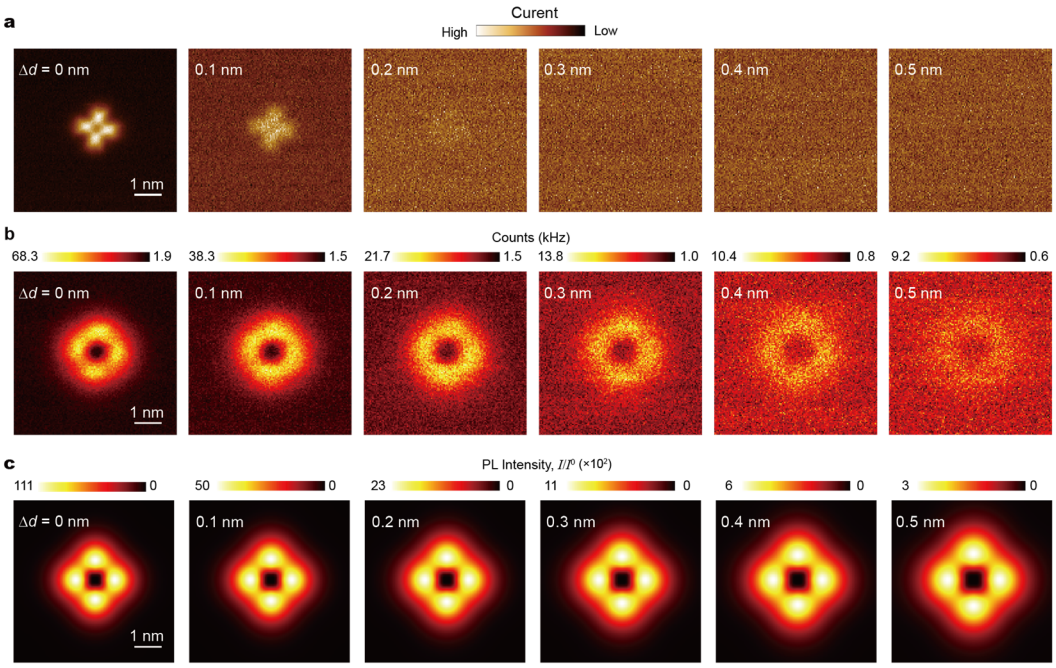

Figure S3 | NCP-enhanced PL imaging maps at different gap distances. a, STM current images of a single ZnPc molecule acquired at different gap distances acquired under the constant-height mode. The initial tip height was regulated at a set-point tunnelling condition of –1 V and 2 pA above the molecular centre, then the feedback loop was switched off, and the images were acquired at different height settings through Z-manipulations (Δd = 0, 0.1, 0.2, 0.3, 0.4, 0.5 nm). **b**, Simultaneously recorded NCP-enhanced PL images corresponding to the STM images in **a**. **c**, Simulated photon images at different gap distances with Δd from 0 to 0.5 nm. The molecule–substrate distance in the theoretical simulations is set to be 1.4 nm and the initial tip–molecule distance is set to be 0.4 nm. A full quantum chemistry description of the degenerated molecular dipoles is adopted. More computational details are given in Section S6.

The sub-nanometre scale NCP field confined by the atomistic protrusion of the tip[7,8] is very sensitive to the gap distance. As shown in Fig. S3, with the increase of the gap distances, the TEPL images become more and more blurred and diffusive, which is supported by the simulated images. Such an observation is consistent with the observed shifts in the lateral peak positions of main-text Fig. 2b and is caused by the less confined plasmonic field in the lateral direction as the gap distance increases. For a molecular transition dipole that is oriented along the horizontal direction (such as ZnPc/3ML-NaCl/Ag(100)), the maximum TEPL intensity will be achieved at the lateral tip position where the dipole can couple most effectively to the horizontal NCP field, allowing for maximal enhancement in both excitation and radiative decay rate. As shown in Fig. S4, when the gap distance is increased, the lateral NCP field along the x direction becomes less confined and the peak position moves to a larger lateral distance x. This leads to the shift in the lateral peak positions in main-text Figs. 2b and 2f.

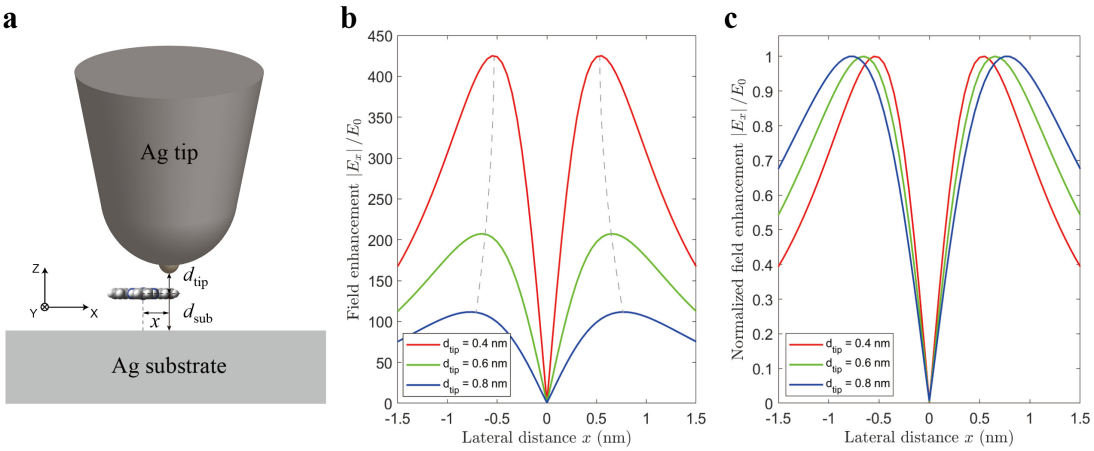

Figure S4 | Dependence of lateral field confinement on tip-molecule distances. a, Schematic for junction geometrical parameters. **b**, **c**, Original and normalized lateral electric field enhancement as a function of lateral distances at different tip−molecule separations. All other parameters used for the calculation are the same as in Fig. S7.

It should be noted that when the tip is lifted further away from the substrate just a little bit (e.g., $\Delta d \geq 0.2$ nm), it is much easier to discern the molecular feature of ZnPc in the TEPL images, than in the corresponding constant-height STM images, as a matter

of fact, the latter becomes featureless when $\Delta d \geq 0.3$ nm. We would like to note that, in this situation, both TERS and STM-induced luminescence (STML) signals also become almost featureless, but the TEPL signal is still quite evident, as shown in Fig. S5a. In other words, even under the out-of-tunnelling regime where TERS and STML fail, the TEPL technique can still provide clear information on the spatial distribution of molecules and their local optical responses (e.g., the quenching effect of local defects), as shown in Fig. S5b−d. Such observations highlight the power and advantage of the TEPL imaging to reveal the features of complex molecular systems over the STM imaging, STML, and TERS techniques, particularly for the out-of-tunnelling regime where STM imaging is no longer possible. The capability of such TEPL technique to image the sample at a relatively large tip–molecule distance will also help to eliminate the tip disturbances, facilitating non-invasive measurements. In addition, the relatively wide range of gap distances available for the TEPL studies allows to make a comprehensive and systematic investigation on the photophysics of fluorescence enhancement and quenching[9-12] as the tip approaches to a molecule until contact, which is difficult to explore using STML technique due to the complications caused by tunnelling current fluctuations and charging of molecules during electron excitations.

Nevertheless, we do not believe that one method is superior to any other since each method has its own advantages and difficulties. On the other hand, TEPL is believed to be fundamentally different from TERS and STML since each method gives access to a different light−matter interaction. TERS is a light scattering process, providing vibrational information associated with the molecular ground state. It does not directly access information about the electronic excited states and therefore cannot be used to explore the important photophysics derived from the fluorescence enhancement and quenching that involves plasmon−exciton coupling. In the case of STML, the excitation source is completely different because it uses localized excitation coming from the highly localized nature of electron tunnelling, allowing to probe the dynamics of electron−molecule interactions without any complexity that may occur due to disturbance of the incident light. However, the intensity of STML is closely related to

tunnelling currents that are exponentially dependent on the gap distance. When the tip approaches very close to a molecule that is electronically decoupled from the metal substrate, the molecular junction becomes highly unstable, resulting in large current fluctuations. Therefore, it is very challenging to explore the photophysical process in a well-defined way in STML. In addition, the charging behaviour involved during the electron excitation may also complicate the study of the photophysical processes with the involvement of charged states. Optically excited TEPL technique gets around all these problems in STML. In TEPL, it is photons that provide the localized excitation. As stated above, TEPL lets one to study photophysics that is not accessible by the other methods. Moreover, our site-dependent measurements of the spectral shift and linewidth broadening (main-text Fig. 4) report the most confined case of the local density of photonic states to date.

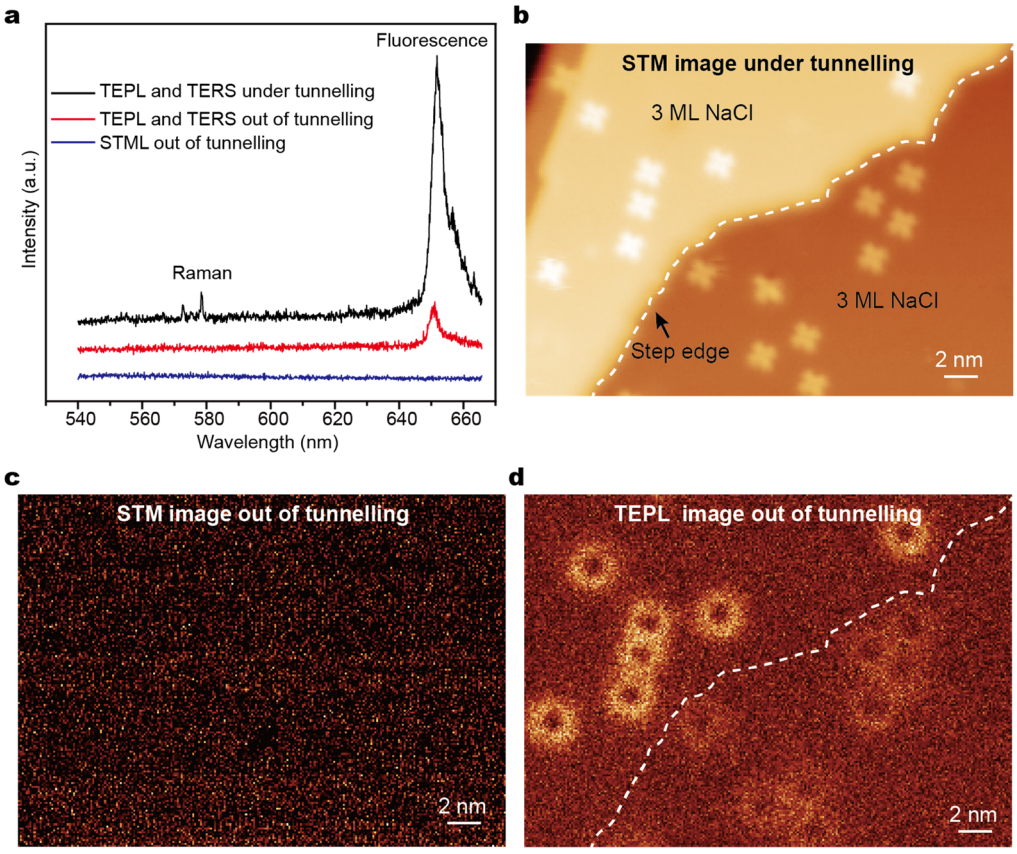

Figure S5 | Comparison of measurement results by TEPL, TERS and STML techniques. **a**, TEPL, TERS and STML spectra acquired at different conditions. Black spectrum shows the

TEPL and TERS signals acquired at −1 V and 2 pA under the tunnelling regime. Red spectrum shows TEPL and TERS signals acquired at the out-of-tunnelling regime, which is retracted by 0.3 nm away from the setpoint condition of −1 V and 2 pA on the ZnPc lobe. Blue spectrum shows the STML signal acquired at the same out-of-tunnelling condition as in the blue spectrum. **b**, STM topographic image acquired in the constant current mode at the tunnelling condition of −1 V and 2 pA. **c**, STM current image acquired in the constant height mode for the same area as **b**, but with the tip retracted by 0.3 nm compared to the tip height in **b**. **d**, Simultaneously recorded TEPL image over the same area in **c**.

S5 Estimation on the tip−molecule distance

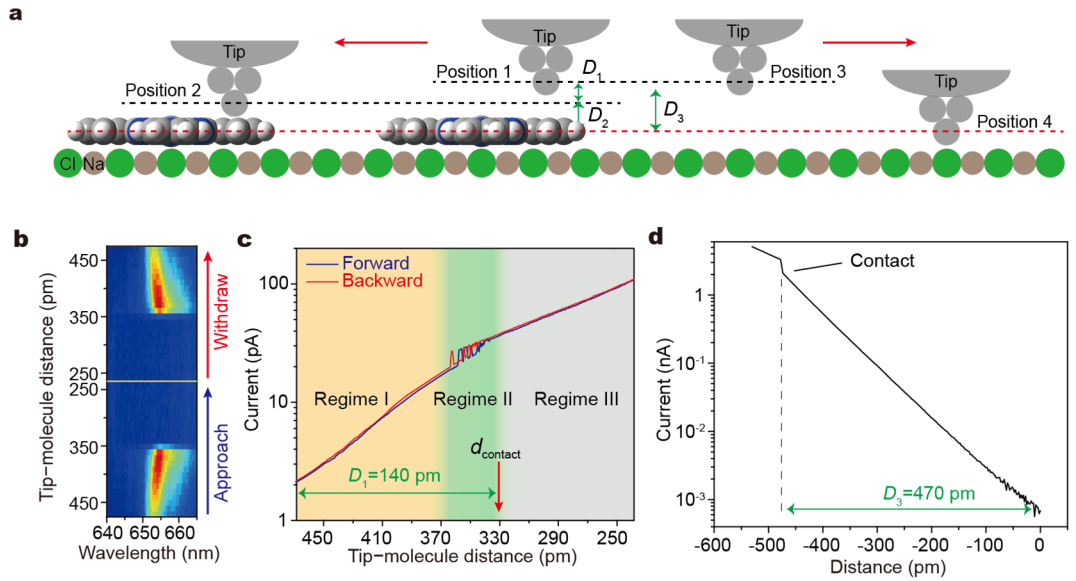

Figure S6 | Tip−molecule distance measurements. a, Schematic illustrating various distances during tip-contact experiments. **b**, Waterfall plot of TEPL spectra for different tip–molecule distances in a tip–molecule contact experiment during the tip approaching and subsequent tip withdrawing processes (Initial set-point condition: −0.7 V, 2 pA; step distance: 10 pm; integration time per spectrum: 1 s). **c**, The measurement on tunnelling currents as a function of the tip−molecule distance. The blue and red line corresponding the tip approaching and withdrawing processes. **d**, The tip trajectory during the approaching to the Cl site of NaCl surface to the contact. The initial tip position (labelled as position 3) is kept at the same as the tip position (labelled as position 1) through the controlled movement of the tip from the molecule to nearby NaCl surface with a constant-height mode.

The precise measurement on the absolute tip–molecule distances is highly challenging because how to define the tip–molecule contact is a scientific question itself. In order to estimate the tip–molecule distances in main-text Fig. 3, we performed controlled tip contact experiments, as illustrated in Fig. S6a. One critical point here is to estimate the tip–molecule distance at the contact point ($d_{contact} = D_2 = D_3 - D_1$), which in our experiments is defined as the position where molecular fluorescence is completely quenched and the tunnelling currents stop fluctuating. Thus, the vertical tip displacement (D_1) between the initial tip position and the contact point can be measured directly through the trajectory of the tip movement, which in this case is about 140 pm (i.e., D_1 =140 pm). Figures S6b and S6c show the evolution of the TEPL spectra with a "mirror" symmetry (Fig. S6b) and the nearly same current variation behaviours during the tip-approaching and subsequent withdrawing processes (Fig. S6c). Such highly controlled and reproducible experiments suggests the intactness of the ZnPc molecule even after tip contacts and the van der Waals-type weak interaction between the tip and the molecule at the contact point.

In order to estimate the tip–molecule distance at the contact point, we record the tip trajectory during the approaching to the nearby NaCl surface using the same initial tip position (position 3) until making a contact. As shown in Fig. S6d, a clear rise in the tunnelling current suggests the contact of the single Ag atom atop the tip apex with the NaCl, which corresponds to a tip approaching distance (D_3) of ~470 pm from the initial tip position. By assuming the distance between the atop-Ag atom and NaCl surface is roughly the same as that between the molecular plane (indicated by the red dash line in Fig. S6a) and the NaCl surface, a tip−molecule distance at the contact point can be estimated to be ~330 pm (i.e., $D_2 = D_3 - D_1 = 470 - 140 = 330$ pm), which is also consistent with the values reported for a van der Waals contact[13,14]. Thus, the absolute tip–molecule distances can be obtained by the sum of the contact distance ($d_{contact}$) and the measured vertical tip displacement (D_1).

We would like to note that the fluctuation near the contact regime is originated from

the molecular motion, rather than from the motion of tip apex atoms, based on the following two facts. First, as shown in Fig. S6d, no current fluctuation behaviour is observed as the same tip gradually approaches to the NaCl surface until a contact is made, which suggests a stable configuration for the tip apex atoms. Second, as shown in Figs. S6b and S6c, the spectral evolution for the tip approaching and tip retraction is highly symmetrical and such experiments are highly controllable and reproducible, which would be difficult to obtain if the fluctuations are caused by the motion of atoms on the uncontrolled tip side.

S6 Theoretical simulations of NCP-enhanced single-molecule PL in the STM junction

The microscopic physical picture for the generation of NCP-enhanced single-molecule PL can be understood as follows: for the excitation process, the photons illuminating the STM junction are converted into highly confined nanocavity plasmons, which effectively excite the molecule; then, the radiative decay of the excited molecule is enhanced by the NCPs, generating far-field photons. Thus, the NCPs play crucial roles in both excitation and emission of the PL processes. In the following, the PL intensity I_{PL} is approximated by the product of the NCP-enhanced excitation rate and the NCP modified quantum efficiency.

In this section, we first describe the geometry of the STM junction and the molecular transition dipole models adopted for our simulations (S6.1). Then, we present the formulas for the excitation rate, radiative decay rate, energy shift and linewidth of the molecular fluorescence in a plasmonic nanocavity (S6.2). This is followed by the simulated photon images of single-molecule photoluminescence with two different transition dipole models (S6.3). We also provide simulations for plasmon enhanced single-molecule photoluminescence with and without an atomistic protrusion at the tip apex (S6.4) as well as for three different substrate situations (S6.5). Finally, we describe the theoretical calculations on the photoluminescence enhancement factor (S6.6) which is associated with the discussion in Section S2.

6.1 Model descriptions

(1) Description of the modelling of the STM junction used for electromagnetic simulations

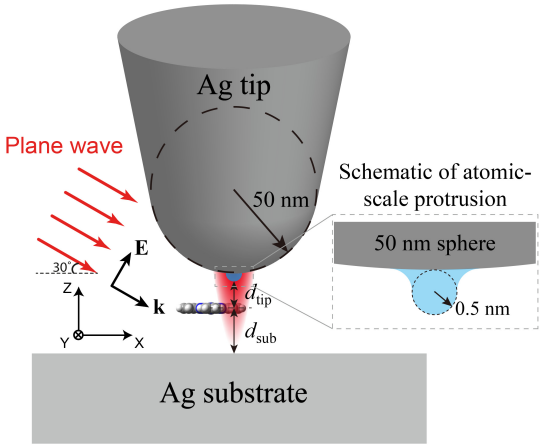

Figure S7 | Schematic showing the geometry of the STM junction used for electromagnetic simulations. Here the tip is modelled as a truncated cone with a height of 200 nm a radius of 50 nm, featuring an additional atomic-scale protrusion at the tip apex. To model the atomistic protrusion, a small sphere with a radius of 0.5 nm is further embedded at the terminal of the large sphere (the geometry of the atomic protrusion used here is shown in the inset). To study the excitation of a single molecule in the nanocavity, the model STM junction is illuminated by a linearly polarized planewave with an energy of 2.33 eV and at an incident angle of 60° with respect to the substrate surface normal. The amplitude of electric field of the incident planewave is set to be 1 V/m. For all following calculations, the distance between the molecule and the substrate is set to be d_{sub} = 1.4 nm.

In order to model the plasmon-enhanced single molecule photoluminescence phenomenon, we carried out electromagnetic simulations based on the boundary element method (BEM)[15] within the quasistatic approximation. As shown in Fig. S7, in our simulation, the STM tip is modelled as a truncated cone with a height of 200 nm and a radius of 50 nm, featuring an additional atomic-scale protrusion at the tip apex. To study the role of an atomistic protrusion at the tip apex on the NCP-enhanced PL process, we further smoothly embed a small sphere with a radius of 0.5 nm at the

terminal of the large sphere (show in the inset of Fig. S7). The substrate is modelled as a cylinder with a radius of 100 nm and a height of 100 nm. The Brendel-Bormann model [16] is used to describe the dielectric responses of the silver tip and the silver substrate. To implement the BEM calculation, the surfaces of the tip and substrate are subdivided into thousands of triangles and quadrilaterals elements. Convergence tests are carried out to make sure that the changes of the boundary elements have negligible effects on the numerical results.

We would like to note that the selection of the tip radius of 0.5 nm is based on the estimated value according to the empirical formula $w \approx \sqrt{Rd}$, which is derived under the assumption of d/R <<1 [17]. Such an assumption does not appear to be well justified for the present nanojunction geometry. However, the current approach, even if beyond the limit of application, reproduces very well the phenomenology observed and the spatial resolution obtained. The spatial resolution for the simulated photon images (Fig. S3c) according to the fitted *R* value, agrees fairly well with the experimental resolution (main-text Figs. 2e and 2f), therefore the empirical formula appears to reflect nicely the scale of local plasmonic field confinement. We would also like to note that a different selection of the prefactor *A* (such as A = 1.41 or 1.57) in $w \approx A\sqrt{Rd}$ will not affect the physical picture that the tip is decorated with an atomic-scale protrusion. Therefore, the simple empirical formula, $w \approx \sqrt{Rd}$, is still used for describing the local plasmonic confinement and estimating the effective tip radius.

(2) Description on modelling of the molecular transition dipole used for electromagnetic simulations

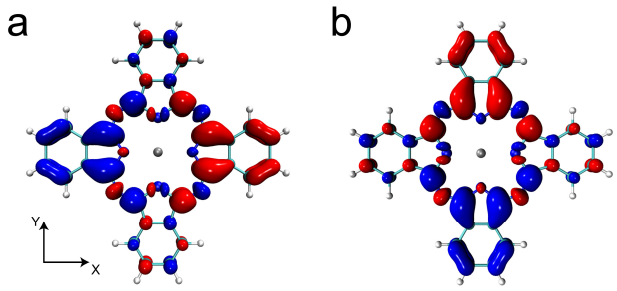

Figure S8 | Transition density distribution of a free ZnPc molecule. a and **b** show the transition density $\rho_{\mathrm{trans},x}(\mathbf{r})$ and $\rho_{\mathrm{trans},y}(\mathbf{r})$ of the two degenerate transitions (i.e., $S_{1,x}\rightarrow S_0$, $S_{1,y}\rightarrow S_0$), respectively. Red and blue colours represent negative and positive charge densities, respectively.

Owing to the D_{4h} symmetry, a free ZnPc molecule possesses two degenerate excited states and, thus, two associated equivalent and orthogonally oriented transition dipoles ($\boldsymbol{\mu}_x$ and $\boldsymbol{\mu}_y$) in the molecular plane. Two kinds of theoretical models are used to describe the transition dipoles. As the simplest approximation, the molecular transitions are modelled as point dipoles locating at the centre of the molecule and pointing parallel to the substrate. This approximation is termed as the point-dipole model (PDM). On the other hand, since the spatial confinement of the inhomogeneous NCP field in the STM junction is believed to be comparable to the dimension of a single ZnPc molecule, the PDM might break down[18] and the finite size of the molecular transition dipole should be considered. Thus, the molecular optical transition is described by the corresponding transition density[19,20], which is obtained by the product of the ground-state $\psi_g(\mathbf{r})$ and excited-state $\psi_{e,\alpha}(\mathbf{r})$ wavefunctions (i.e., $\rho_{\mathrm{trans},\alpha}(\mathbf{r})=\psi^*_{\mathrm{e},\alpha}(\mathbf{r})\psi_{\mathrm{g}}(\mathbf{r})$, $(\alpha=x,y)$) (Fig. S8), where the transition density of a free ZnPc molecule is calculated with the time-dependent density-functional theory (TD-DFT) at the B3LYP/6-311G(d) level using the Gaussian 16 software package [21]. In addition, according to the TD-DFT calculation, the transition dipole moment of ZnPc molecule ($|\boldsymbol{\mu}_x|$ or $|\boldsymbol{\mu}_y|$) is ~7.4 Debye, which corresponds to a spontaneous emission rate of $\Gamma^0 \sim 0.041$ μeV in vacuum. The second

model is termed as the transition-density model (TDM) based on a full quantum chemistry description of the degenerated molecular dipoles, which is the model used for all the computation results presented in the main text. For both PDM and TDM, the energy of the molecular transition is set to be 1.9 eV.

S6.2 Theoretical expressions of the excitation rate, radiative decay rate, total decay rate and energy shift for a single molecule in a plasmonic nanocavity

Considering the two different treatments on the molecular transition dipole described above, we present the theoretical expressions of the excitation rate, radiative decay rate, total decay rate and energy shift for a single molecule based on PDM and TDM, respectively.

(1) Excitation rate, radiative decay rate, total decay rate and energy shift calculated under the point dipole model approximation

According to the Fermi golden rule[22], in the PDM, the excitation rate of the α-th dipole ($\alpha = x, y$) of a single molecule under planewave illumination can be expressed as

$$w_{\mathrm{exc},\alpha}(\mathbf{R}_{\mathrm{tip}}) \propto \frac{2\pi}{\hbar}\left|\boldsymbol{\mu}_{\alpha} \cdot \mathbf{E}_{\mathrm{pw}}(\mathbf{R}_{\mathrm{tip}}, \mathbf{r}_0)\right|^2,$$

Where $\mathbf{E}_{\mathrm{pw}}(\mathbf{R}_{\mathrm{tip}}, \mathbf{r}_0)$ is the electric field at the position of the point dipole $\mathbf{r}_0$ in the nanocavity under planewave illumination when the tip is placed at $\mathbf{R}_{\mathrm{tip}}$.

For a molecule in an inhomogeneous plasmonic nanocavity, its transition dipole experiences additional forces from its own field, which is the field that acts back to the molecule after scattered by the nanocavity. Such self-interaction can result in the optical dressing of molecular excited states and thus leads to the tip-position dependent modifications on the transition energy and decay rate. The spectral shift $\Delta\omega$ and the total decay rate Γ^{tot} (approximately equal to the linewidth[22]) of the point dipole in the nanocavity can be expressed as [23,24]

$$\frac{\Delta\omega_\alpha(\mathbf{R}_{\text{tip}})}{\Gamma^0} \approx -\frac{3\pi\epsilon_0 c^3}{\omega_0^3 \left|\boldsymbol{\mu}_\alpha\right|^2} \times \text{Re}\left[\boldsymbol{\mu}_\alpha^* \cdot \mathbf{E}_{\text{scat},\alpha}(\mathbf{R}_{\text{tip}}, \mathbf{r}_0)\right],$$
$$\frac{\Gamma_\alpha^{\text{tot}}(\mathbf{R}_{\text{tip}})}{\Gamma^0} \approx 1 + \frac{6\pi\epsilon_0 c^3}{\omega_0^3 \left|\boldsymbol{\mu}_\alpha\right|^2} \times \text{Im}\left[\boldsymbol{\mu}_\alpha^* \cdot \mathbf{E}_{\text{scat},\alpha}(\mathbf{R}_{\text{tip}}, \mathbf{r}_0)\right],$$

where $\mathbf{E}_{\text{scat},\alpha}(\mathbf{R}_{\text{tip}}, \mathbf{r}_0)$ is the α-th component of the scattered field at the position of the molecule $\mathbf{r}_0$ produced by $\boldsymbol{\mu}_\alpha$ when the tip is placed at $\mathbf{R}_{\text{tip}}$, $\Gamma^0 = \frac{\omega_0^3 \left|\boldsymbol{\mu}_\alpha\right|^2}{3\pi\hbar\epsilon_0 c^3}$ is the decay rate of the point dipole in vacuum, ω_0 is the energy of the dipole and ϵ_0 is the vacuum permittivity. We note that, within the PDM, the imaginary part of self-interaction, described by $\Gamma^{\text{tot}}(\mathbf{R}_{\text{tip}}) \propto \text{Im}\left[\boldsymbol{\mu}^* \cdot \mathbf{E}_{\text{scat}}(\mathbf{R}_{\text{tip}}, \mathbf{r}_0)\right] \propto \rho_{\text{PDOS}}(\mathbf{r}_0)$, is associated with the decay rate, which can be enhanced by the Purcell effect due to the change in the PDOS ($\rho_{\text{PDOS}}(\mathbf{r}_0)$) and can lead to the linewidth broadening. Therefore, if the molecule is assumed as a point dipole, then the linewidth mapping will give direct information on the spatial distribution of the PDOS projected on the dipole.

The radiative decay rate of a point dipole in the nanocavity can be expressed in terms of the effective dipole moment of the total nanocavity-molecule system [15,25,26]

$$\frac{\Gamma_\alpha^{\text{rad}}}{\Gamma^0} \approx \frac{\left|\boldsymbol{\mu}_\alpha + \boldsymbol{\mu}_{\text{ind},\alpha}^{\text{PDM}}\right|^2}{\left|\boldsymbol{\mu}_\alpha\right|^2},$$

where $\boldsymbol{\mu}_{\text{ind},\alpha}^{\text{PDM}}$ represents the dipole moment of the nanocavity induced by the point dipole $\boldsymbol{\mu}_\alpha$.

(2) Excitation rate, radiative decay rate, total decay rate and energy shift calculated under the transition-density model approximation

The expressions for the TDM can be derived in a similar way to that for the PDM. In the TDM approximation, the excitation rate of the α-th dipole of a single molecule under planewave illumination can be expressed as [19,20]

$$w_{\text{exc},\alpha}(\mathbf{R}_{\text{tip}}) \propto \frac{2\pi}{\hbar}\left|\int \rho_{\text{trans},\alpha}(\mathbf{r}')\phi_{\text{pw,tot}}(\mathbf{R}_{\text{tip}}, \mathbf{r}')d^3\mathbf{r}'\right|^2,$$

where $\phi_{\mathrm{pw}}(\mathbf{R}_{\mathrm{tip}},\mathbf{r}')$ is the electrostatic potential at position $\mathbf{r}'$ under planewave illumination when the tip is placed at $\mathbf{R}_{\mathrm{tip}}$, $\rho_{\mathrm{trans},\alpha}(\mathbf{r}')$ is the transition density of the α-th transition dipole. The spectral shift and total decay rate can be expressed as [19,20]

$$\frac{\Delta\omega_\alpha(\mathbf{R}_{\mathrm{tip}})}{\Gamma^0} \approx \frac{3\pi\epsilon_0 c^3}{\omega_0^3\left|\boldsymbol{\mu}_\alpha\right|^2} \times \mathrm{Re}\left[\int \rho_{\mathrm{trans},\alpha}(\mathbf{r}')\phi_{\mathrm{scat},\alpha}(\mathbf{R}_{\mathrm{tip}},\mathbf{r}')d^3\mathbf{r}'\right],$$

$$\frac{\Gamma_\alpha^{\mathrm{tot}}(\mathbf{R}_{\mathrm{tip}})}{\Gamma^0} \approx 1 + \frac{6\pi\epsilon_0 c^3}{\omega_0^3\left|\boldsymbol{\mu}_\alpha\right|^2} \times \left|\mathrm{Im}\left[\int \rho_{\mathrm{trans},\alpha}(\mathbf{r}')\phi_{\mathrm{scat},\alpha}(\mathbf{R}_{\mathrm{tip}},\mathbf{r}')d^3\mathbf{r}'\right]\right|,$$

where $\phi_{\mathrm{scat},\alpha}(\mathbf{R}_{\mathrm{tip}},\mathbf{r}')$ is the scattered potential at $\mathbf{r}'$ produced by $\rho_{\mathrm{trans},\alpha}(\mathbf{r}')$ when the tip is placed at $\mathbf{R}_{\mathrm{tip}}$, $\Gamma^0 = \dfrac{\omega_0^3\left|\int \rho_{\mathrm{trans},\alpha}(\mathbf{r}')\mathbf{r}'d^3\mathbf{r}'\right|^2}{3\pi\hbar\epsilon_0 c^3}$ is the decay rate of the transition density in vacuum and is much smaller than the total decay rate (Γ^{tot}) in a plasmonic nanocavity. The nanocavity-enhanced radiative decay rate for the molecule can be expressed as

$$\frac{\Gamma_\alpha^{\mathrm{rad}}}{\Gamma^0} \approx \frac{\left|\int \rho_{\mathrm{trans},\alpha}(\mathbf{r}')\mathbf{r}'d^3\mathbf{r}' + \boldsymbol{\mu}_{\mathrm{ind},\alpha}^{\mathrm{TDM}}\right|^2}{\left|\int \rho_{\mathrm{trans},\alpha}(\mathbf{r}')\mathbf{r}'d^3\mathbf{r}'\right|^2},$$

where $\boldsymbol{\mu}_{\mathrm{ind},\alpha}^{\mathrm{TDM}}$ is the dipole moment of the nanocavity induced by the molecular transition density $\rho_{\mathrm{trans},\alpha}(\mathbf{r}')$.

Once both the radiative and total decay rates are calculated according to the above expressions, the quantum efficiency $\eta_\alpha(\mathbf{R}_{\mathrm{tip}})$ can thus be obtained via $\eta_\alpha(\mathbf{R}_{\mathrm{tip}}) = \dfrac{\Gamma_\alpha^{\mathrm{rad}}(\mathbf{R}_{\mathrm{tip}})}{\Gamma_\alpha^{\mathrm{tot}}(\mathbf{R}_{\mathrm{tip}})}$. Then, the calculated PL intensity contributed from $\boldsymbol{\mu}_\alpha$ $(\alpha = x, y)$ can be obtained by the product of the NCP-enhanced excitation rate $w_{\mathrm{exc},\alpha}(\mathbf{R}_{\mathrm{tip}})$ and the quantum efficiency $\eta_\alpha(\mathbf{R}_{\mathrm{tip}})$, namely, $I_\alpha(\mathbf{R}_{\mathrm{tip}}) = w_{\mathrm{exc},\alpha}(\mathbf{R}_{\mathrm{tip}}) \times \eta_\alpha(\mathbf{R}_{\mathrm{tip}})$. Since the ZnPc molecule possess two equivalent transition dipoles and these two degenerated transitions are treated independently, the simulated total photon intensity for a specific tip position ($\mathbf{R}_{\mathrm{tip}}$) is the sum of the

calculated PL intensity of each dipole, namely, $I(\mathbf{R}_{\text{tip}}) = I_x(\mathbf{R}_{\text{tip}}) + I_y(\mathbf{R}_{\text{tip}})$.

Considering the presence of two sets of spectral peak shifts ($\Delta\omega(\mathbf{R}_{\text{tip}})$) and linewidth broadenings ($\Delta\Gamma(\mathbf{R}_{\text{tip}})$) for each tip position contributed from $\boldsymbol{\mu}_x$ and $\boldsymbol{\mu}_y$ respectively, we take the maximum value of them at each pixel to simulate the spectral images, namely,

$$\Delta\omega(\mathbf{R}_{\text{tip}}) = \max\{\Delta\omega_x(\mathbf{R}_{\text{tip}}), \Delta\omega_y(\mathbf{R}_{\text{tip}})\},$$
$$\Delta\Gamma(\mathbf{R}_{\text{tip}}) = \max\{\Gamma_x^{\text{tot}}(\mathbf{R}_{\text{tip}}) - \Gamma^0, \Gamma_y^{\text{tot}}(\mathbf{R}_{\text{tip}}) - \Gamma^0\}$$
$$\approx \max\{\Gamma_x^{\text{tot}}(\mathbf{R}_{\text{tip}}), \Gamma_y^{\text{tot}}(\mathbf{R}_{\text{tip}})\}.$$

Such a treatment was adopted to reflect the dominant contribution from the stronger interaction at each position between the plasmonic dipole and molecular transition dipole ($\boldsymbol{\mu}_x$ or $\boldsymbol{\mu}_y$). As shown in main-text Fig. 4e and 4f, the features of the simulated images for the spectral shifts $\Delta\omega(\mathbf{R}_{\text{tip}})$ and linewidth broadenings $\Delta\Gamma(\mathbf{R}_{\text{tip}})$ are in fair agreement with the experimental images in term of the positions and numbers of maxima and nodes. It should be noted that the precise values of the spectral shifts and broadenings depend substantially on the actual distribution of the NCP field and the molecular transition density in the STM junction. However, the NCP field is very sensitive to the actual configuration achieved (particularly regarding the structure of the atomistic protrusion[7,8]) and the dielectric constants of the plasmonic nanocavity. All these parameters are not well-defined in such nanoscopic environment. Although the plasmon−molecule interactions are mainly responsible for such linewidth broadenings, there are other factors such as dephasing[22] and molecule−NaCl substrate interactions that are not taken into account in the present simulation, but may make smaller contributions to the linewidths observed experimentally. In addition, also not considered in the present calculation is the nonlocal dielectric response that may provide additional contributions to the linewidth broadening for very short gap distances[27]. In this sense, the discrepancy between the experimental and theoretical values highlights the demand for more sophisticated theories to treat complex real systems. Our results provide unprecedented data for benchmarking the theoretical

understanding of molecular-scale optical processes, and are likely to trigger a new series of efforts in both experiments and theories to explore and understand light−matter interactions at a new frontier.

S6.3 Simulations on the photon images of single-molecule TEPL with two different transition dipole models

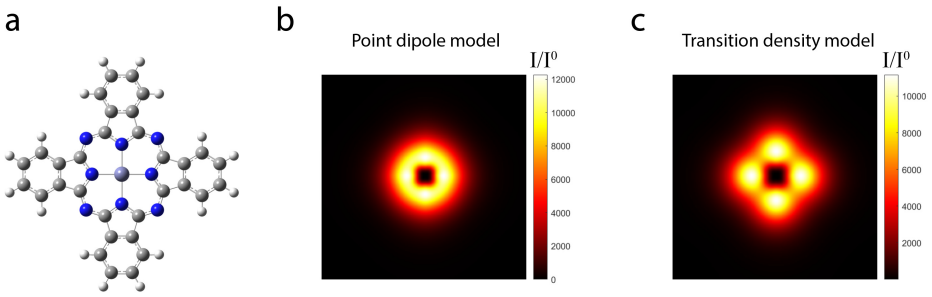

Figure S9 | Simulated photon images for a single ZnPc molecule using the PDM and the TDM. a, Atomic structure of a free ZnPc molecule. **b**, Simulated photon image for the PDM in which the molecule is simplified as two orthogonal point dipoles lying parallel to the substrate. **c**, Simulated photon image using the TDM. The distance between the tip and the ZnPc molecule in the simulation is set to be 0.4 nm. The size of both figures are 6 nm × 6 nm. The calculated photon image for the PDM resembles a nearly-perfect circular ring, while the calculated photon image for the TDM exhibits a clear four-lobe pattern, which is in better agreement with the experimentally observed photon image in main-text Fig. 1d. In a word, the point-dipole model fails to describe the experimental imaging pattern and the spatial distribution of the transition density within a molecule should be taken into account.

S6.4 Electromagnetic simulations for the plasmon enhanced single-molecule PL intensity with and without an atomistic protrusion at the tip apex

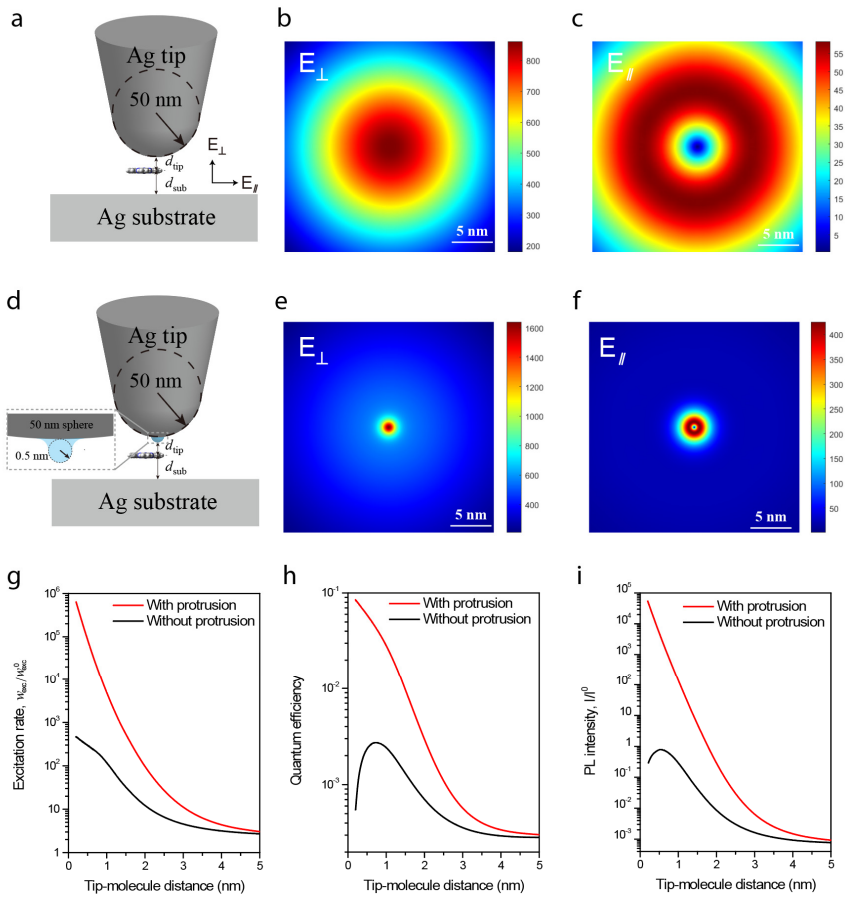

Figure S10 | Simulations for the electric fields under planewave excitation and molecular emission properties for different tip structures. a, Schematic for the configuration of the STM junction, where a Ag tip is placed above the lobe of ZnPc molecule. **b** and **c**, Horizontal ($E_{//}$) and vertical ($E_{\perp}$) components of the local electric fields simulated for the junction in **a**. **d**, Schematic for the configuration of the STM junction, where a Ag tip with an atomistic protrusion at the apex is placed above the lobe of ZnPc molecule. **e** and **f**, Horizontal ($E_{//}$) and vertical ($E_{\perp}$) components of the local electric field simulated for the junction in **d**. **g–i**, The calculated excitation rate, quantum efficiency and TEPL intensity as a function of tip–molecule distances for the two different tip structures shown in **a** and **d**. The lateral distance between the molecular centre and the tip apex is set to be 0.8 nm. As illustrated in **i**, for a tip without an atomistic protrusion, the calculated TEPL intensity tends to decrease at small tip–molecule distances when the tip approaches to a ZnPc emitter above the Ag substrate. On the contrary, for a tip with an atomistic protrusion, strong and ever-increasing photoluminescence is observed for very short tip–molecule distances. Such a difference is probably due to a strong and highly localized NCP field caused by the additional atomic-scale lightning rod effect of the atomistic

protrusion at the tip apex[8] (main-text Fig. 3d), which can offer very large plasmonic enhancement to the radiative decay rate and resultant quantum efficiency. In addition, the significant lateral field components around the atomistic protrusion is equally important, since the generated lateral field can effectively excite the horizontally oriented transition dipole of a nearby ZnPc molecule. We would like to note that the simulation results presented in main-text Figs. 3c and 3d are obtained using the same TDM model and the same junction geometry illustrated in **d**, namely, a full quantum chemistry description of the degenerated molecular dipoles is adopted and the lateral displacement between the tip apex and the molecular centre is set to be 0.8 nm.

S6.5 Electromagnetic simulations of plasmon-enhanced single-molecule PL behaviours for three different substrate situations

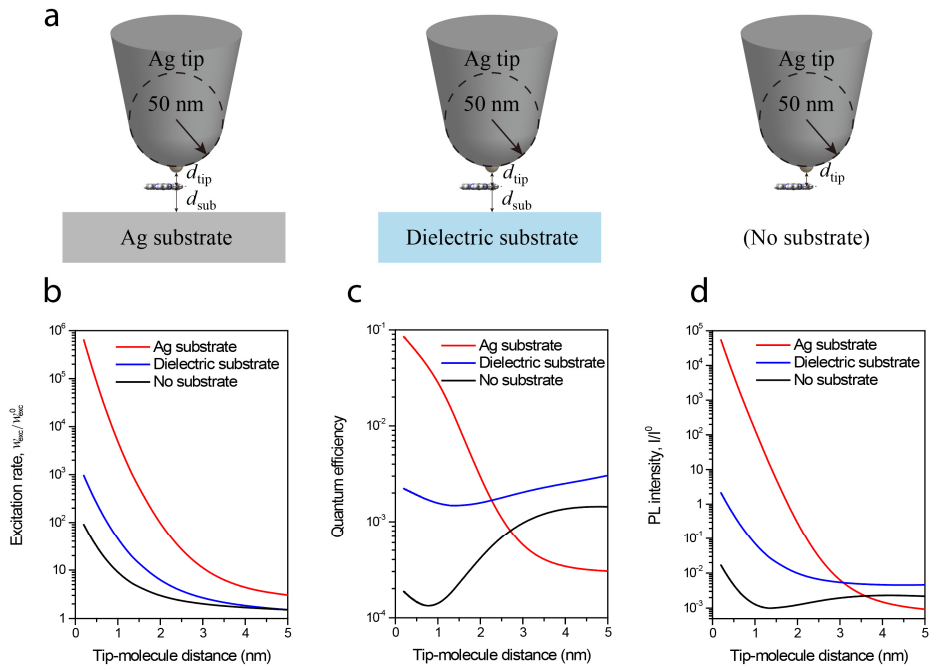

Figure S11 | Simulations of the single-molecule TEPL behaviours for three different substrate situations. a, Schematics showing plasmon-enhanced single-molecule PL for three different substrate situations. Left: a Ag substrate; Middle: a dielectric substrate (with an adopted dielectric constant $\epsilon_r = 3$, which is close to that of glass or NaCl materials); Right: no substrate. **b**–**d**, Excitation rate, quantum efficiency and PL intensity for the molecule in the

above three different substrate situations in **a.** The lateral distance between the molecular centre and the tip apex is set to be 0.8 nm. The simulation results indicate that the presence of a metallic substrate and the resultant NCP field are very important for the observation of enhanced single-molecule PL. The calculated fluorescence intensities are weaker by ~4 orders of magnitude if a dielectric substrate (e.g., NaCl or glass) is used instead of the Ag substrate. In addition, for a substrate-free situation (i.e., no NCP), the molecular fluorescence is practically quenched, consistent with the results in the literature for emitters in close proximity to open nanoantennas[9].

S6.6 Theoretical calculation on the TEPL enhancement factor

In order to understand the giant TEPL enhancement factor of ~10^8 estimated in Section S2, we calculated the enhancement factor by performing the simulations on the decay rates of a single ZnPc in different electromagnetic environments. For a single ZnPc placed 1.4 nm above the Ag substrate but without a tip, the excitation enhancement is as small as ~0.4 and the quantum efficiency is down to ~3×10^{-4} due to the greatly enhanced non-radiative decay rates caused by the metal substrate, leading to a strongly quenched PL intensity by a factor of ~1×10^{-4} compared with that of a single ZnPc in vacuum. However, for a single ZnPc placed in a nanocavity between a Ag tip with an atomic protrusion and Ag substrate, the excitation rate is enhanced by a factor of ~2×10^5 and the quantum efficiency is ~0.07, leading to an enhancement factor of ~1×10^4 compared with the PL intensity for a single ZnPc placed in vacuum (here the vertical tip−molecule distance is set to be 0.4 nm and the lateral distance between the molecular centre and the tip apex is set to be 0.8 nm). Thus, an enhancement factor of ~10^8 can be obtained for the PL intensity of a single ZnPc in the NCP field with respect to that of a single ZnPc placed close to the substrate in a tip-free situation, which is very close to the experimentally estimated value in Section S2.

S7 More discussion on the spectroscopic imaging of ZnPc as well as its spectral shift and linewidth

(1) More discussion on the spatial resolution of spectroscopic imaging

In main-text Fig. 1d, the photon image was obtained by recording at each lateral scan pixel the photon intensity from a single photon avalanche diode (SPAD) with the use of a bandpass filter (655 nm ± 7.5 nm) to select the major emission peak of ZnPc. The spatial resolution of the TEPL imaging is defined by the 10%–90% optical contrast in the photon emission intensity across a molecule, which is estimated to be ~0.8 nm (main-text Fig. 1e). The same spatial resolution can be realized for spectroscopic imaging in which a TEPL spectrum is acquired at each pixel during scanning. Figure S12a shows the spatial distribution of emission intensities for the TEPL spectroscopic imaging over a single ZnPc molecule, which is the same experiment for the results presented in main-text Fig. 4. As shown by the lineprofile analysis in Fig. S12b, the spatial resolution is also 0.8 nm. Such a sub-nanometre resolved spectroscopic imaging ability allows us to map the molecular exciton energy and linewidth at sub-molecular resolution (main-text Figs. 4c and 4d). We emphasize that all the photon images presented in this work were acquired at the constant-height mode.

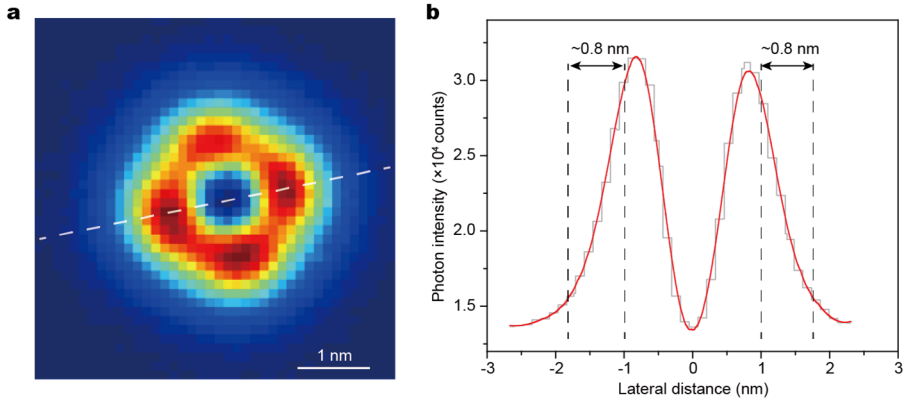

Figure S12 | Spatial distribution of emission intensities for the spectroscopic imaging of ZnPc. a, Emission intensity map obtained from the experimental spectroscopic image, which was acquired for the same area in main-text Fig. 4a (5 nm × 5 nm, 40 × 40 pixels, 2 s per pixel, integration over 651.4−653.3 nm). **b,** Intensity profile analysis for the line trace shown in **a**.

(2) More discussion on the spectral shifts in the emission spectra of ZnPc

The spatial distribution feature presented in main-text Fig. 4c for the spectral shifts is believed not to be caused by the Stark effect. As shown in Fig. S13, when the bias

voltage is changed from −1.5 V to −0.001 V at a fixed gap distance, the peak energy is shifted by ~2 meV, suggesting that the Stark shift does affect the absolute peak position. However, in main-text Fig. 4, all the spectra were collected with a constant gap distance at a fixed bias voltage. As a result, the DC electric field associated with the applied bias voltage is constant over the molecule during the measurement, and the Stark effect is believed to be similar for every molecular position. In addition, the amount of shift (~1 meV at −1 V) caused by the Stark effect is much smaller than the photonic Lamb shift of about 7 meV observed. Therefore, the Stark effect is not expected to affect the overall spatial distribution of peak energy shifts, and thus such an effect was not considered in the present theoretical simulations.

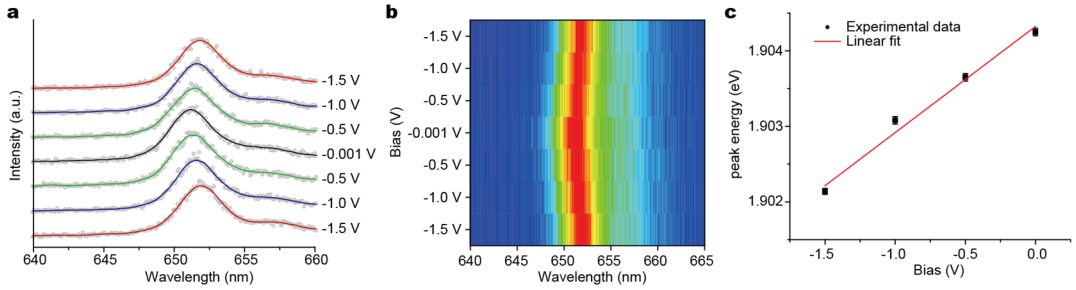

Figure S13 | Bias-dependent measurements of TEPL spectra at a fixed gap distance. a, TEPL spectra from a single ZnPc/3ML-NaCl/Ag(100) as a function of bias with a fixed gap distance regulated at −2 V and 2 pA over the molecular lobe. **b**, waterfall plot of **a**. **c**, Peak energies as a function of bias obtained from **a**.

We also believe that the spatial distribution of spectral shifts in main-text Fig. 4 is not caused by the deformation of the molecule. The spectroscopic imaging presented in main-text Fig. 4 was carried out in a constant height mode at a height regulated under −1 V and 2 pA over the molecular lobe, which corresponds to a tip−molecule distance of ~470 pm (Figs. S6c). Such a distance is much larger than the van der Waals distance, and as a result, the chemical interaction between the tip and molecule is expected to be very weak, not enough to induce the deformation of the molecule.

(3) More discussion on the spectral linewidth in the emission spectra of ZnPc

As regards the spectral linewidth in the emission spectra, according to our previous analysis on the STML spectra of ZnPc molecules[22], the broad linewidth of an isolated ZnPc molecule on 3ML-NaCl/Ag(100) (~10.8 meV) is mainly composed of the contribution from the molecular self-interaction induced by the plasmonic nanocavity (~8.5 meV) and the dephasing contribution (~2.3 meV). The former also contains the contribution from the interaction of the molecule with the metal substrate (~0.3 meV), the latter is probably due to the interactions of molecular exciton with intramolecular vibrations and the NaCl substrate. The same analysis can be applied to account for the linewidth broadening of the TEPL spectra of an isolated ZnPc molecule on 3ML-NaCl/Ag(100). The dephasing contribution is considered to be essentially identical for the same molecule on the same substrate, namely 2.3 meV. Therefore, the observed linewidth of ~10 meV for the TEPL spectra in main-text Fig. 1c has a major contribution from the molecular self-interaction induced by the plasmonic nanocavity (~7.7 meV).

We would like to note that the linewidth on the order of 10 meV shown in main-text Fig. 4d suggests a lifetime of molecular excited states around several hundreds of femtoseconds. Such a viewpoint is now further supported by the second-order photon correlation measurement on an isolated single ZnPc molecule excited by photons using our recently developed TEPL technique. No photon antibunching dips were observed, suggesting that the molecular lifetime is much shorter than the time resolution of our (HBT) setup (~80 ps) (Otherwise, photon antibunching dips should show up for a single-molecule experiment). Since the clear difference between the electron excitation (STML) and photon excitation (TEPL) is the occurrence of a transient charged state in the former (involving a three-state model), while the molecule remains neutral during photon excitation (involving a two-state model), the long time constant of 0.48 ns observed previously for the HBT measurements in STML[14] is more likely to correlate with the existence of a transient charged intermediate state. The understanding of the antibunching behaviour and associated time constants certainly deserves further theoretical and experimental studies.

References

1 Zhang, C. *et al.* Fabrication of silver tips for scanning tunneling microscope induced luminescence. *Rev. Sci. Instrum.* **82**, 083101 (2011).

2 Kazuma, E., Jung, J., Ueba, H., Trenary, M. & Kim, Y. Real-space and real-time observation of a plasmon-induced chemical reaction of a single molecule. *Science* **360**, 521-526 (2018).

3 Huang, Y. P. *et al.* Shell-isolated tip-enhanced Raman and fluorescence spectroscopy. *Angew. Chem.* **130**, 7645-7649 (2018).

4 Raunio, G., Almqvist, L. & Stedman, R. Phonon dispersion relations in NaCl. *Phys. Rev.* **178**, 1496 (1969).

5 Imada, H. *et al.* Single-molecule investigation of energy dynamics in a coupled plasmon-exciton system. *Phys. Rev. Lett.* **119**, 013901 (2017).

6 Dong, Z. *et al.* Generation of molecular hot electroluminescence by resonant nanocavity plasmons. *Nat. Photon.* **4**, 50 (2010).

7 Trautmann, S. *et al.* A classical description of subnanometer resolution by atomic features in metallic structures. *Nanoscale* **9**, 391-401 (2017).

8 Urbieta, M. *et al.* Atomic-scale lightning rod effect in plasmonic picocavities: a classical view to a quantum effect. *ACS Nano* **12**, 585-595 (2018).

9 Anger, P., Bharadwaj, P. & Novotny, L. Enhancement and quenching of single-molecule fluorescence. *Phys. Rev. Lett.* **96**, 113002 (2006).

10 Kühn, S., Håkanson, U., Rogobete, L. & Sandoghdar, V. Enhancement of single-molecule fluorescence using a gold nanoparticle as an optical nanoantenna. *Phys. Rev. Lett.* **97**, 017402 (2006).

11 Fu, B., Flynn, J. D., Isaacoff, B. P., Rowland, D. J. & Biteen, J. S. Super-resolving the distance-dependent plasmon-enhanced fluorescence of single dye and fluorescent protein molecules. *J. Phys. Chem. C* **119**, 19350-19358 (2015).

12 Li, J.-F., Li, C.-Y. & Aroca, R. F. Plasmon-enhanced fluorescence spectroscopy. *Chem. Soc. Rev.* **46**, 3962-3979 (2017).

13 Wagner, C. *et al.* Non-additivity of molecule-surface van der Waals potentials from force measurements. *Nat. Commun.* **5**, 5568 (2014).

14 Zhang, L. *et al.* Electrically driven single-photon emission from an isolated single molecule. *Nat. Commun.* **8**, 580 (2017).

15 Hohenester, U. & Trügler, A. MNPBEM–A Matlab toolbox for the simulation of plasmonic nanoparticles. *Comput. Phys. Commun.* **183**, 370-381 (2012).

16 Rakić, A. D., Djurišić, A. B., Elazar, J. M. & Majewski, M. L. Optical properties of metallic films for vertical-cavity optoelectronic devices. *Appl. Opt.* **37**, 5271-5283 (1998).

17 Rendell, R. & Scalapino, D. Surface plasmons confined by microstructures on tunnel junctions. *Phys. Rev. B* **24**, 3276-3294 (1981).

18 Zhang, Y., Dong, Z.-C. & Aizpurua, J. Influence of the chemical structure on molecular light emission in strongly localized plasmonic fields. *J. Phys. Chem. C* **124**, 4674-4683 (2020).

19 Neuman, T. s., Esteban, R., Casanova, D., García-Vidal, F. J. & Aizpurua, J. Coupling of molecular emitters and plasmonic cavities beyond the point-dipole approximation. *Nano Lett.* **18**, 2358-2364 (2018).

20 Aguilar-Galindo, F., Díaz-Tendero, S. & Borisov, A. G. Electronic structure effects in the coupling of a single molecule with a plasmonic antenna. *J. Phys. Chem. C* **123**, 4446-4456 (2019).

21 Gaussian 16 Rev. C.01 (Wallingford, CT, 2016).

22 Luo, Y. *et al.* Electrically driven single-photon superradiance from molecular chains in a plasmonic nanocavity. *Phys. Rev. Lett.* **122**, 233901 (2019).

23 Novotny, L. & Hecht, B. *Principles of Nano-Optics*. (Cambridge university press, 2012).

24 Chance, R., Prock, A. & Silbey, R. Frequency shifts of an electric-dipole transition near a partially reflecting surface. *Phys. Rev. A* **12**, 1448-1452 (1975).

25 Sukharev, M., Freifeld, N. & Nitzan, A. Numerical calculations of radiative and non-radiative relaxation of molecules near metal particles. *J. Phys. Chem. C* **118**, 10545-

10551 (2014).

26 Hohenester, U. & Trugler, A. Interaction of single molecules with metallic nanoparticles. *IEEE J. Sel. Top. Quantum Electr.* **14**, 1430-1440 (2008).

27 Johansson, P., Xu, H. & Käll, M. Surface-enhanced Raman scattering and fluorescence near metal nanoparticles. *Phys. Rev. B* **72**, 035427 (2005).